2026 IEEE International Conference on Robotics and Automation (ICRA 2026)
June 1-5, 2026. Vienna, Austria

USV with Interfacial Pumping for Efficient Microplastics Removal

Stephan Wagner[1], Yicong Fu[1], Sunghwan Jung[2], and Kirstin Petersen[1*]

***Abstract*— Microplastics that accumulate at the air–water interface pose urgent ecological and health risks. However, existing sampling and collection methods based on surface trawls are hindered by hydrodynamic resistance. We present the first in-motion characterization of an interfacial pump mounted on a small uncrewed surface vehicle (USV) to actively draw surface water into an onboard filter. Experiments combining thruster-driven forward motion with the undulating pump show that low thruster output and moderate pumping frequency maximize particles captured per unit energy, balancing the ram effect of forward speed with the lateral suction of the pump. Scaled towing tests reveal that the pontoon cross-section strongly influences intake flow, indicating that streamlined profiles can further boost filtration efficiency. Finally, flow-visualization confirms that the pump's ability to generate far-field suction without bulk mixing—previously demonstrated only in static tests—persists while the USV is in motion. These results establish interfacial pumping as a promising bio-inspired strategy for manual and autonomous microplastics collection, and highlight design parameters that can guide future development of distributed, high-coverage sampling platforms.**

I. Introduction

Estimates suggest that 5–13 million tonnes of plastic enter our oceans each year [1], originating from tires, synthetic textiles, consumer products, and many other sources. Plastic use is expected to triple over the next three decades [2], while recycling has become increasingly intractable. The chemical diversity of plastics, multilayer packaging, and widespread additives mean that U.S. recycling facilities achieve reuse rates of only $\sim$6% [3]. As these plastics fragment into micro-scale particles, they become pervasive in rivers, lakes, and oceans and accumulate across trophic levels with dire consequences for ecosystems and human health [4]. These issues have led scientists to call for improved strategies to monitor and remove microplastics from aquatic systems.

In this paper, we investigate a low-cost, small-scale uncrewed surface vehicle (USV) designed to filter microplastics (Fig. 1). We focus on removing microplastics from the water surface, where buoyant particles frequently accumulate [5]. Once mixed into the bulk by turbulence, aggregation, and bio-fouling, recovery becomes far more difficult. Although commercial devices exist for removing larger plastic debris from rivers and harbors, these do not effectively capture microplastics. Even approaches specifically targeting microplastics using towed micro-scale filters are inefficient because hydrodynamic resistance diverts flow around the filter media rather than through them. To overcome this, we integrate an undulating interfacial pump, inspired by a discretized rotary helix mechanism that has been shown in previous works [6], [7]. Specifically, Joo *et al.* [8] and Pandey *et al.* [7] demonstrated that this mechanism actively draws in surface water from the far-field without mixing with the bulk. We hypothesize that integrating this mechanism with our USV will increase efficacy and energy efficiency of microplastics capture by manually-controlled and autonomous robotic agents, while minimizing drag and mixing effects.

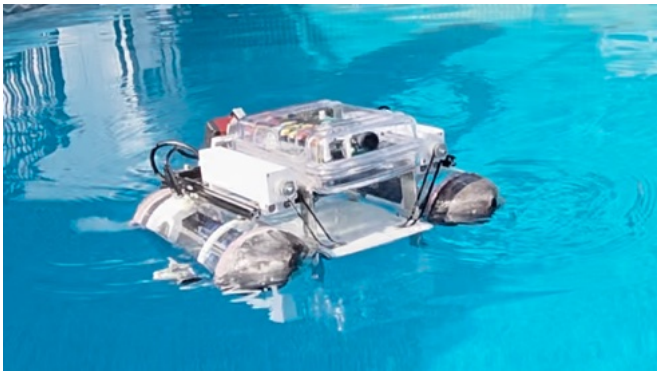

Fig. 1. Integration of interfacial pump with a small-scale USV for efficient filtration of microplastics from the water surface.

Typically, microplastics are sampled at the water surface using meshes or skimming nets in so-called manta or neuston trawls [9] and then analyzed in standardized lab workflows. These methods have significant throughput limits, however, and research has shown that they can undercount buoyant particles by up to 30 times due to hydrodynamics during collection [10]. Pump-underway intake systems mounted on ships improve coverage significantly, but only sample subsurface water [11]. To increase spatiotemporal resolution, recent work has turned to autonomous approaches. In the closest related work [12], Faltynkova *et al.* demonstrated a USV coupled with hyperspectral imaging to assess aquatic microplastics. While their focus was on the vessel autonomy and microplastics analysis, we instead focus on the detailed design parameters for improving the efficiency of the flow intake needed for sampling and filtration at scale. In addition, we focus on a low-cost and compact design to allow for lab-scale studies. Beyond the lab, targeting future deployment in lakes and rivers, our USV can withstand water immersion, has low clearance for deployment in shallow water, and the agility to withstand mild currents.

This work was funded by NOAA grant # NA24OARX417C0598-T1-01.
[1]College of Engineering, Cornell University, Ithaca, NY 14853, USA (sw933@cornell.edu, yf357@cornell.edu, kirstin@cornell.edu)
[2]College of Agriculture and Life Sciences, Cornell University, Ithaca, NY 14853, USA (sunnyjsh@cornell.edu)

In the following sections, we (i) describe the integration of interfacial pumping into a pontoon-boat USV, (ii) characterize the motion of the robot with and without a microplastics filter, (iii) evaluate how the pump operation overcomes filter resistance, including an analysis of efficiency in terms of power consumption versus flow rate, and (iv) discuss how to optimize the hull design parameters. Our results highlight the potential of active pumping to scale microplastics filtration in natural waters.

A supplementary video shows key experimental results.

II. System Design

We designed and constructed our USV using many off-the-shelf parts in addition to a few custom, mostly 3D printed ones. The total build cost of the robot is roughly 1,000 USD.

A. Buoyant USV Platform

Our USV is a pontoon boat platform, in which two cylindrical hulls, made of thin, transparent tubing from ClearTec and fitted with pointed end caps, provide stable flotation. Using thin and inexpensive tubing material avoids the complexity and weight of molded or 3D printed pontoon geometry, while allowing flexibility in the length of the pontoons during construction and ample interior space to carry batteries and other electronics below the robot's center of mass. The hulls in the design presented here are 0.09 m in diameter, 0.3 m in length (L), and are spaced apart to leave a 0.12 m gap. We chose these dimensions to limit the robot's horizontal bounding box to 0.3×0.3 m while providing buoyancy against the 2.5 kg mass of the full assembly. We also kept the robot's height within 0.2 m, only half of which lies above the water. This low-profile design is particularly suited to iteration and experimentation because we can test individual and multiple robots in tanks and pools in a lab setting. In calm weather, we can also operate the USV outdoors, where its compact size will allow future use in tight and cluttered spaces with minimal disturbance to flora and fauna.

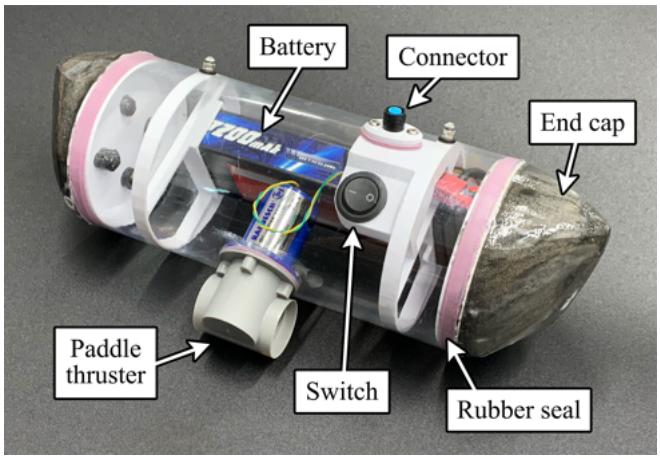

Fig. 2. **One of two pontoons used to form the buoyant USV platform.** The transparent tubing allows easy assessment of the components. The on/off switch breaks connection with the battery and can be toggled by pressing through the tubing. The connector fits a watertight cable that carries power and signals to and from the electronics case.

Each of the robot's pontoons (Fig. 2) carries a Zeee 7.4V, 7200 mAh, Li-Po battery, a power switch, and a 25 mm ID, bidirectional, 7.4V, brushed DC paddle thruster—a so-called "bow" thruster—from Harbor Models. The system's small scale limited reasonable choice of thrusters to brushed motors because brushless drivers, while more efficient, would have required considerably larger housings and interior pontoon volume. The end caps are molded from rigid FOAM-iT!™ 10 urethane foam from Smooth-On, and sealed with custom molded urethane rubber gaskets. These caps are easily removed for fast battery changes in the field. We mounted the thrusters midway along the length of the pontoons and well below the water line for minimal disturbance to particles at the water surface. We aligned the thrusters' housings so that their force output is parallel to the direction of forward travel. With this arrangement, we can turn the robot about its central vertical axis, making it highly maneuverable and agile in water. The batteries can power the system for 3–4 hours under computational and mechanical load, and twice that duration when idling.

We connected the pontoons using T-slotted aluminum beams to form a rigid platform that carries the robot's electronics. We then attached two flat, U-shaped aluminum bars to the rigid structure such that their ends, as four columns or "fins", extend down from the beam platform and just past the bottom of the pontoons (Fig. 3 (a) and (b)). The fins provide support to mount the pump at the water line and serve as legs for the USV when on land. We chose aluminum as the fin material because of its rigidity, but also because of its thermal conductivity, which additionally allows the fins to passively direct heat away from the robot's electronics and into the water (the fins are visible inside the electronics enclosure in Fig. 6 (a)).

B. Pump

The primary payload onboard the USV is the interfacial pump: a flexible dual-helix-driven undulator positioned just under the water surface (Fig. 3 (a) and (b)). The undulator is a thin membrane, which we 3D printed with flexible TPU filament. We sized the pump to take up the entire gap between the pontoons, thereby maximizing water and microplastics intake. We chose an undulation amplitude of 0.015 m; roughly the same as the depth of water above the pump, so that the membrane remains fully submerged during pumping operation.

We lined the underside of the undulator with a series of ribs (Fig. 3 (b)), except for a short posterior section that acts as a passive tail. The ribs, oriented perpendicularly to the USV's direction of travel, allow the membrane to be highly flexible in its longitudinal or fore-aft axis, yet resistant to buckling in its lateral or port-starboard axis. We cut channels through the ribs at their lateral ends to insert two helical shafts that support and actively drive the undulator. These helices are mirrored in their handedness and rotate in phase

to induce sinusoidal motion of the membrane. By using two helices, we avoid lateral rocking of the undulator.

The active part of the pump has a traveling wave profile and kinematics that are determined by the helix amplitude. When placed just under the free water surface, the undulator forms a thin pumping channel. As the membrane's top surface pushes against or pulls away from the air-water interface (Fig. 3 (c)), alternating high and low pressure zones are created to induce a suction flow similar to that in peristaltic pumps [7]. This flow can be statically visualized by a pulsatile surface particle trajectory (Fig. 4). Locally, this mechanism generates a directional mean flow along the wave propagation parallel to the surface. The zero-gradient velocity boundary condition at the free surface guarantees directional movement of the interfacial fluid, generating solid particle transport over the pump.

The passive part of the membrane enables a trailing edge amplitude much greater than that of the helical shafts. Fig. 3 (c) shows the fluid behavior around the undulator, including counter-rotating trailing edge vortices, whose circulation strength scales quadratically with the trailing edge amplitude [13]. These vortices are shed during each stroke of the tail, where low pressure cores encourage pumping flow to the wake region.

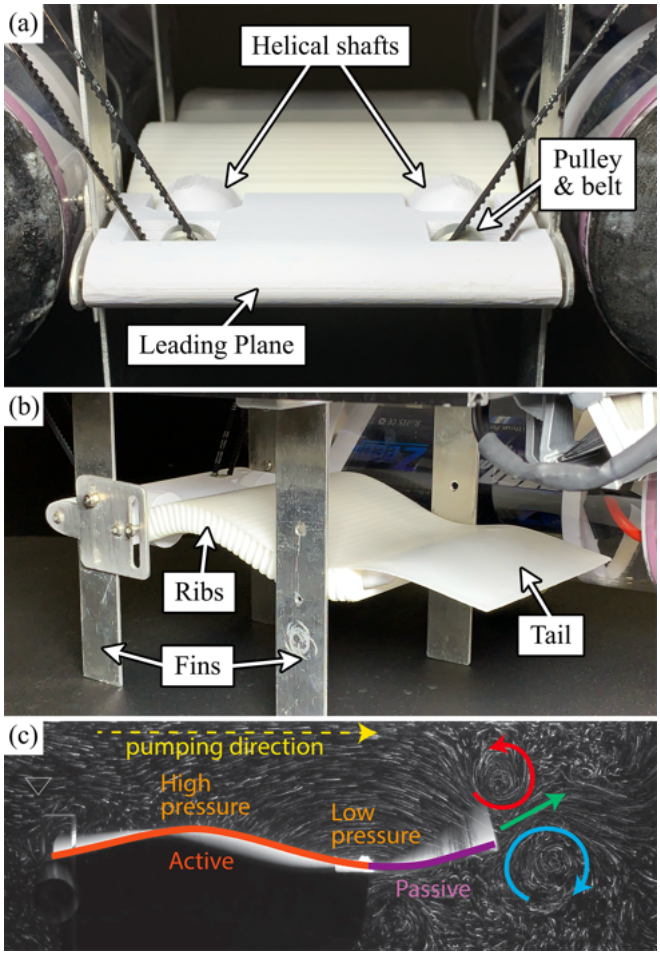

Fig. 3. **Thin-membrane undulating pump.** The flexible membrane is supported by mirrored helical shafts on the left and right sides. The helices are driven by pulleys and timing belts. (a) Front view. (b) Rear-side view. (c) Side-view of experimental flow visualization using neutrally buoyant hollow glass spheres (Dantec), with pumping mechanisms annotated.

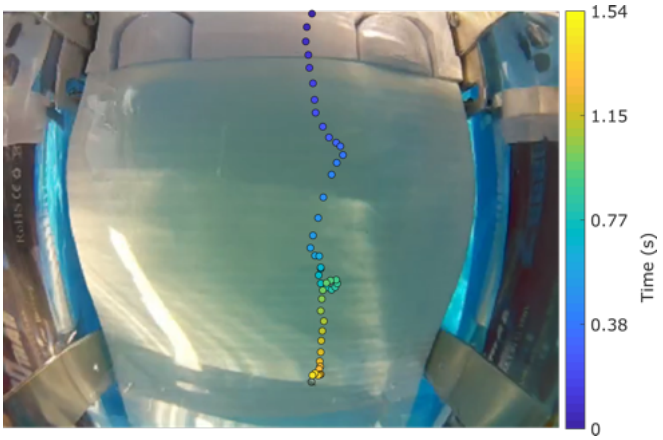

Fig. 4. **Particle tracking in downward facing camera view.** Grass seed tracked as it moves across the pump surface during undulation at 50% PWM, mounted on the freely moving USV.

The undulating pump is inherently different from traditional sink-flow pumps that can form a vertical vortex line extending from the pump nozzle to the free surface, thereby drawing air and surface particles into the bulk. Our pump, conversely, transports microplastics floating in the interfacial water near the robot without vertical mixing.

In front of the undulator, we mounted the pump's helices via steel shafts to a streamlined plane. The plane is then pinned to the aluminum fins extending from the rigid platform above. This arrangement firmly holds the entire undulating pumping mechanism below the water surface. When we drive the mechanism at the air-water interface, the undulator draws surface water into and through the space between the pontoons from vehicle-scale distances ahead of the robot.

To drive the helical shafts, we positioned two 20.4:1, high-power, 6V, brushed DC gearmotors from Pololu on either side of the electronics case above the water line. The geared motors, which we placed inside custom, 3D printed, water-resistant enclosures with O-rings and rotary seals, provide enough speed and torque to drive the pump, via pulleys and timing belts, in a frequency (f) range of 2.5–6.5 Hz.

We chose to drive the pump using two separate motors to achieve greater pumping power and finer frequency control than what one motor would have allowed. We chose to mount the motors above the water line and use pulleys and belts to transmit rotation to the pump to minimize the necessary mechanical components that would induce drag or block either the pump opening at the water surface or the view from the forward-facing camera inside the electronics case. We synchronize the pump motors in software using 980 encoder pulses per revolution generated by Hall-effect sensors at the output shafts.

C. Filter

To mimic the effect of a neuston trawl, we attached a 0.11 m wide planar mesh filter behind the undulating pump (Fig. 5). The mesh size is 333 µm, the upper bound on microplastics particle diameter set by NOAA [14] in 2009.

We have yet to test and optimize the efficacy of the planar filter. The current design is meant to demonstrate one possible filtering approach that also allows for automated cleaning. We hold the filter mesh in a frame that is free to slide within a set of rails at a 30° angle from vertical. We chose this angle to slightly reduce drag added by the filter when the robot is moving, though optimization of the exact inclination will require further dedicated testing. To eliminate drag entirely, a servo motor can raise and lower the filter above and below the water line, respectively. Particles drawn in by the pump and directed through the space between the pontoons can be caught by the filter before exiting that space. The filtration is aided by sticking effects when the particles are small enough or when there is considerable salt content in the water, as would be the case with seawater. When periodically lifted, the sliding filter moves against a small set of brushes that clear collected microplastics from the mesh and deposit them in a simple holding chamber.

The filtering approach described here demonstrates a particle sampling strategy, rather than thorough particle removal. For our analysis of microplastic collection performance and efficiency later on, we study the blocking effect of the filter on the flow of particles. The filter design itself is a suggested mechanism for removal that will be the subject of improvement and testing in future work.

D. Control

We control the USV with a Raspberry Pi 5 (RPi) housed in a watertight, acrylic Pelican case and mounted above the pontoons and therefore well above the water line (Fig. 6 (a)). One of the pontoon batteries is entirely dedicated to powering the control circuitry and the RPi, the power consumption of which is not yet optimized but does not factor into our later pumping efficiency analysis. To facilitate heat removal from the enclosed RPi, we modified the case to allow the robot's aluminum cooling fins to pass through the acrylic walls and past the electronics inside. A small fan circulates the air inside the enclosure.

We chose the RPi 5 because it is a capable single-board computer that can operate independently or be commanded remotely over WiFi, but also because it supports two camera connections via its CSI FPC headers. The cameras are housed in the same transparent electronics case as the RPi. One camera points forward (Fig. 6 (b)) to view the environment ahead of the robot, the other points downward (Fig. 6 (c)) to monitor the water drawn in by the pump for analysis (Fig. 4).

The RPi's GPIO pins deliver PWM to two MC33926 dual-motor controllers from Pololu, which drive the thrusters and pump motors, respectively. An Adafruit INA260 I^2C power sensor records the battery power drained by the thrusters and pump. To synchronize the pump motors, we implemented a PID controller in C++ on the RPi, which combines the pulses from each motor to continuously adjust the respective output PWM channels. This synchronization reliably maintains in-phase rotation of the helices and symmetry in the undulator's motion while the pump is active.

Finally, we connected a Bitcraze Lighthouse Deck positioning receiver to the RPi's serial communication pins, which allows the robot to locate with millimeter precision. The Lighthouse Deck detects two rotating, orthogonally planar, infrared laser sweeps emitted by Lighthouse beacons placed at the edges of the workspace. We chose the Lighthouse system over motion capture—another common indoor positioning approach—because of its portability. When testing our robot in and outside of the lab, we can easily transport the Lighthouse beacons and quickly set up a workspace over water. Since the Lighthouse Deck performs localization

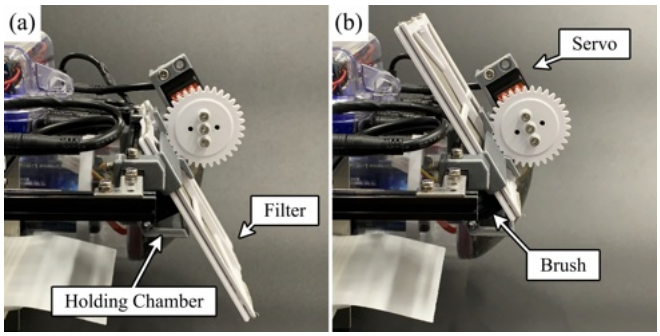

Fig. 5. **Mesh filter mechanism mounted at 30° from vertical behind the pump and depth-adjustable by servo.** The brush and holding chamber are visible below the left side of the filter frame. (a) Filter engaged in the down configuration. (b) Filter disengaged in the up configuration.

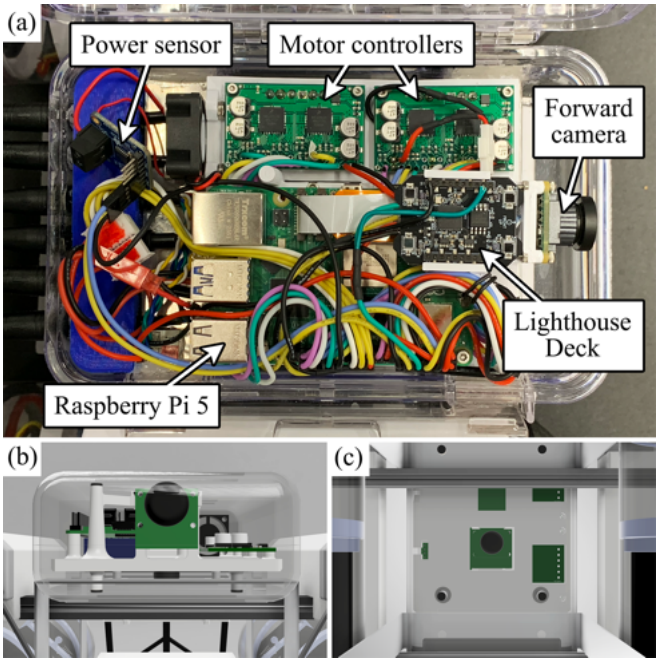

Fig. 6. **Control electronics in watertight acrylic case.** (a) Top view of the electronics case, lid open. The RPi is partially obstructed by wiring and the Lighthouse Deck. (b) Front view CAD rendering of the forward facing camera. (c) Bottom view CAD rendering of the downward facing camera.

onboard the USV based only on the infrared sweeps generated by the beacons, the positioning data emulates a GPS signal, while orientation is provided by an IMU. In future autonomous deployments of our robots, the Lighthouse Deck can be swapped for dedicated GPS hardware.

III. USV Motion Characteristics

Our 0.3×0.3 m USV is small enough to operate in a lab setting, where we conduct experiments using tanks or small wading pools. To test the robot's speed and agility, however, we use larger facilities like fixed indoor and outdoor swimming pools (Fig. 1) that provide enough space to bring the boat up to full speed via its thrusters.

From outdoor pool testing of the thrusters at low-drag configuration (without the filter engaged), we determined the USV's continuous straight-line speed to be in the range of 0.28–0.49 m/s, corresponding to 50–100% pulse width modulation and 22.5–45.3 W of thruster power consumption, respectively. We learned from this testing that the boat, given its scale, is highly influenced by water currents, indicating a need for feedback control on surface velocity in the future. Additionally, the robot can turn on-axis at a maximum rate of 180°/s. Fig. 7 shows the relationship between speed and power at different combinations of thruster- and pump-based propulsion when the filter is engaged. The pump's ability to drive the robot forward is limited because it draws water only at the surface. The pump alone also cannot provide steering. Therefore, the thrusters are necessary to control the robot's position in water, while the pump is best suited at affecting surface particles.

Fig. 7 shows that the power requirement to reach a particular speed is higher when using a combination of thrusters and pump propulsion compared to using the thrusters alone. This is to be expected, as the pump is less efficient at propelling the boat than the thrusters. Fig. 7 also shows that

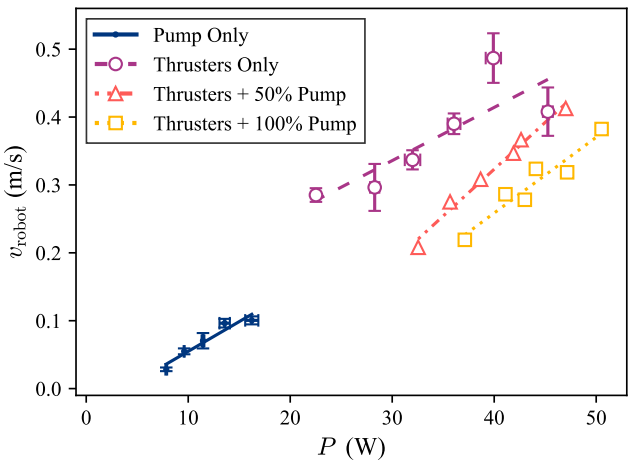

Fig. 7. **Robot speed in water due to power input to the thrusters and/or pump.** In all shown trials, the filter was engaged. We performed five repetitions for the pump only and thruster only configurations, as indicated by the error bars on those series. The pump alone achieved very low speeds, while the thrusters alone achieved the highest speeds.

the maximum achievable speed drops when both the thrusters and the pump are active, and more so with increasing PWM. This occurs because both sets of motors are powered by the same battery, which, while rated for heavy loads, does experience voltage sag. As we show later, operating both thrusters and pump at top speed is not efficient; therefore, this issue plays no major role in our design.

IV. Thruster-Induced Flow

When we propel the USV using only the thrusters, microplastics collection functions like a traditional, towed neuston trawl. The particles ram into the filter and get sifted from the water. Intuitively, the filtering flow rate strongly depends on the robot's shape and speed. However, the filter also adds resistance, or drag, which depends on the size and porosity of the mesh material. Since we could not reasonably seed large swimming pools with tracer particles to quantify the effects of robot shape and speed, and resistance of the filter, we instead conducted experiments in an indoor pool in our lab. We also conducted experiments by towing a scaled-down and simplified model of the USV and its filter.

For the towing tests, we used a 30%-scale model of the USV in a shallow tank (50×40×5 cm). This scaled model was not fitted with functioning thrusters or interfacial pump. Instead, the towing action simulated mean flow through the inter-pontoon space as would be generated by either the thrusters, the pump, or a combination of both, allowing us to quantify the effects of the robot's geometry on the flow rate. We connected the front of the model to one end of a monofilament fishing line and tied the other end to a 2 g weight. By allowing the weight to fall, the model was towed across the water surface in the tank and flow through the model was generated in repeatable fashion. For tracer particles, we seeded the water surface with white hydrophobic glass microspheres from Fasco Epoxies (diameter ≈ 70 μm). Additional weights on the model allowed us to tune the submergence depth. When released, the model accelerated to a terminal travel velocity ($v_r = 0.14$ m/s) as the weight fell. A Photron Fastcam Nova S6 high-speed camera fixed in the lab frame recorded a top-down view at 125 fps. Using PIVlab [15], we performed particle image velocimetry (PIV) to obtain surface particle velocities while applying a moving mask on the model. Due to low Stokes numbers of the surface particles, we approximate the surface flow velocities ($\mathbf{u} = [u_x, u_y]$) to be equal to the particle velocities.

We define useful flow rate (Q) as the surface 2D inflow between the pontoon tips, which we calculate as $Q \equiv \int_{\text{left}}^{\text{right}} -u_x^{\text{rel}}\, dy$, where u_x^{rel} is the fluid velocity relative to the moving robot (Fig. 8 (a)).

With the filter disengaged from the water (Fig. 8 (b)), we evaluated slip-wall pontoons that do not divert flow laterally (i.e. pontoons with a solid-liquid interface which is smooth enough to achieve negligibly thin boundary layers). Here, the theoretical maximum Q is simply $v_r w = 89.62$ cm^2/s, where $w = 6.4$ cm is the inlet width. With the real pontoon geometry, flow experienced stagnation and boundary layers,

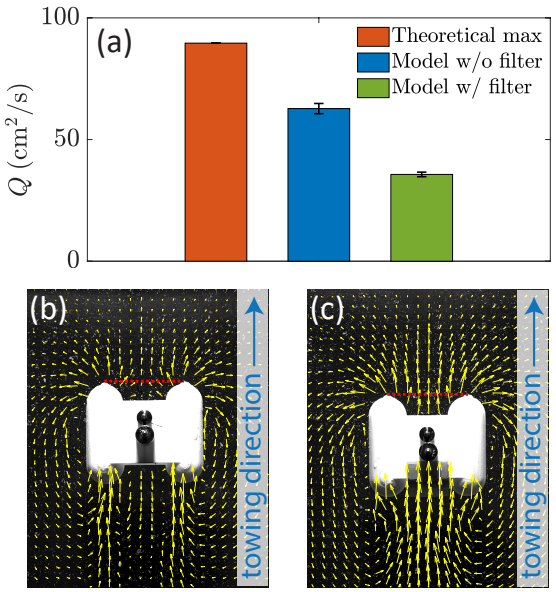

Fig. 8. **Effects of robot shape and filter condition on thruster-induced flow rate estimated from small-scale towing experiments.** Note that the small-scale model is not fitted with an interfacial pump. (a) Flow rate at various conditions. (b) Instantaneous flow field around a forward-moving model without a filter or pump. (c) Instantaneous flow field around a forward-moving model with a filter but without a pump. **Note:** The model is moving vertically upward in the image (blue arrow). The red dashed line represents the pump inlet. The yellow vectors show fluid velocities with respect to the fixed lab frame.

and hence a reduced Q at 62.72 cm^2/s. This indicates potential for a more streamlined pontoon shape.

With the filter engaged in the water (Fig. 8 (c)), additional pressure loss reduced Q to 35.67 cm^2/s. The filter increased blockage to the flow, resulting in larger u_x in the v_r direction. This led to a smaller u_x^{rel} magnitude and a reduced Q. As a first-order approximation, we assume that the full-scale robot, operating at higher travel velocity v_r, shares a self-similar flow field as the small towing model, while also assuming that the filter proportional blockage of flow remains the same across scales. Finally, the instantaneous surface flow velocity $\mathbf{u}$ with respect to the fixed lab frame in Fig. 8 (c) is linearly scaled by the USV's speed ratio $\beta = v_r^{\text{target}}/v_r^{\text{tow}}$ to inform our pumping efficiency model.

V. Pump-Induced Flow

Without thruster-induced ramming, the undulating pump can generate flow as described in Section IV. The pump's macroscopic flow field resembles a potential flow doublet, with one side acting as the sink inlet and the opposite side as the source outlet.

For the indoor pool experiments, we fixed the robot inside a 2.4×1.2 m pool filled with just enough water to induce buoyancy at the pontoons. This depth represents the untethered operating condition, but also allowed us to neglect the effect of unsteady vertical bobbing, a behavior we observed being consistently induced by the undulator in deeper water. By fixing the robot and using only the interfacial pump to

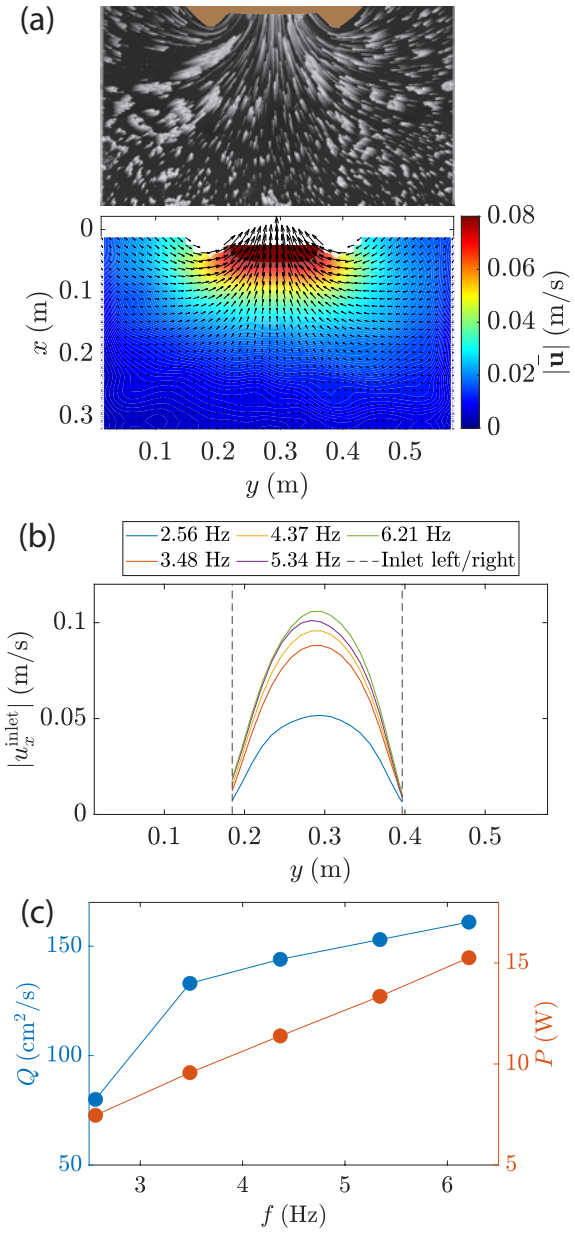

Fig. 9. **Flow induced by the undulating pump.** (a) Overlaid particle trajectories and the associated time-averaged suction velocity field around the robot inlet (brown mask). Parameter y is the horizontal distance across the analyzed flow field. (b) Inlet pumping velocity profiles at various frequencies. (c) Flow rate and power consumption at various frequencies.

affect the water surface, we could isolate the flow generated by the pump for a range of undulator frequencies f, set via PWM input to the pump motors. We seeded the water surface with conventional glitter (diameter $\approx$ 1 mm) and recorded the flow with a video camera at 30 fps for 90 seconds. We selected 30 seconds of video from the middle of each trial, where a steady flow of glitter particles had been reached, but before all particles had dispersed, and computed time-averaged surface flow velocity $\mathbf{u}$ using PIV. Fig. 9 (a) shows how the surface particles were effectively drawn into the inlet with increasing speed as they approached the undulator. As

the doublet analogy predicts, the pump not only creates an additional flow rate, but also gathers the particles from the far-field and from both sides of the robot.

We extracted streamwise velocity profiles at the inlet to compute a useful flow rate Q (Fig.9 (b)). Across all undulator frequencies f, the streamwise velocity reaches a maximum at the center of the channel and nearly zero at the pontoon tips, suggesting that the pontoons have an effect on the flow rate. As f increases, both Q and power usage P increase, but Q does not increase in a linear fashion (Fig. 9 (c)). Similar non-linear trends have been reported at low Reynolds (Re) numbers [7], but further fluid dynamics analysis is needed to explain this phenomenon in our turbulent regime. This non-linearity also potentially renders the efficiency non-linear with f, indicating a possible intermediate optimal condition.

In our current USV design, the pump spans the entire gap between the pontoons, thus 3D edge effects like roll-up vortices can be neglected. With this quasi-2D assumption, we expect flow rate Q to scale linearly with the width of the undulator. The amplitude of the undulating wave may increase Q but also induce drag and surface disturbance.

Because the passive tail portion at the rear of the undulator bends due to fluid forces, tuning the actuation and damping with its resonance frequency can maximize the trailing edge amplitude to create stronger pumping flow through the shedding vortex rings [16]. To that end, we believe there is potential to further optimize the pump via material selection, dimension, and actuation.

VI. Thruster and Pump-Induced Flow

We evaluate the system performance of our USV by the particle capture efficiency (η), which we define as the number of particles the robot can collect per unit of energy spent. Figs. 7 and 9 show parametric performance studies at several increments of v_r ranging between 0 m/s and the robot's top speed of 0.49 m/s, and five increments of f that we tested experimentally by driving the pump in the range of 50–100% PWM. To assess the resulting performances, we built a simple numerical simulator.

In this simulation, we seeded a "water" surface with particles in a uniform grid of 5 mm spacing across a domain of 0.7×0.36 m upstream of the USV. We simulated particle trajectories driven by the superpositioned fluid velocity with respect to a frame fixed on the cruising robot. We advanced the trajectories using a fourth-order Runge–Kutta (RK4) integrator with a time step of 0.01 seconds. Particles that cross the inlet plane within the physical width of the filter (0.11 m) were considered captured. We then define the capture rate as the ratio between the number of captured particles (N_{captured}) and the total number seeded (N_{total}). Finally, we calculated the system performance η as N_{captured}/P to identify optimal operational conditions.

Since the USV speed v_r combines propulsion from the thrusters and the pump, we subtracted the pump-only speed (Fig. 7) from v_r to decouple the effects of the thrusters and the pump. Fig. 10 shows that the horizontal data space is skewed, with some negative values of $v_r^{\text{thrusters}}$. This

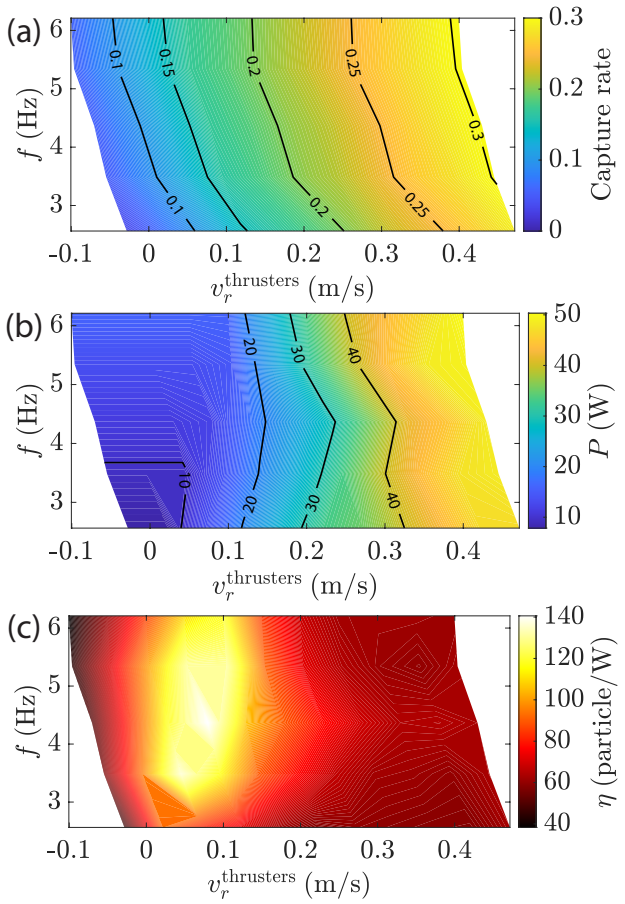

Fig. 10. **Particle capture performance.** (a) Simulated capture rate. (b) experimentally inter/extrapolated power usage. (c) efficiency at various combinations of thruster-induced robot velocity and pump undulation frequency.

is expected, because rearward thrust would be required to counteract the pump's effects if we aim to hold the robot's position steady. The capture rate seems to increase both with thruster output and pumping frequency, but thrusters' contribution is more significant (Fig. 10 (a)). The total power usage shows a less monotonic trend (Fig. 10 (b)), which creates a local efficiency maxima at the intermediate $v_r^{\text{thrusters}}$ - f range (Fig. 10 (c)). This indicates that, to reach peak performance, our current USV design is best operated at low thruster output and moderate pumping frequency. This result is reasonable because (i) if thruster output is too low, we do not benefit from the ramming effect as shown in Fig. 8; (ii) if thruster output is too high, the pump is unable to sufficiently concentrate the particles; (iii) if the pumping frequency is too low, filter blockage is not improved; and (iv) if the pumping frequency is too high, mechanical load becomes a significant burden.

Our results show that our dual-mechanism system outperforms traditional neuston trawls by actively collecting far-field particles and driving them to the filter, and that system performance is optimal while cruising at moderate speed to maximize energy efficiency.

VII. Discussion of Hull Design Parameters

Our analysis shows that the pontoons can be reshaped to improve passive flow intake as the USV drives forward, but only at the cost of size and maneuverability. Hull drag adds three main contributions: (i) surface friction due to fluid viscosity, (ii) form drag due to anterior stagnation and posterior wake flow separation, and (iii) wave drag due to surface waves.

Given our current waterline length of 0.3 m and our optimal thruster-induced velocity of roughly 0.1 m/s (Fig. 10 (c)), our robot operates in high Reynolds range ($Re = v_r L/\nu$, where ν is the kinematic viscosity of water) of around 45,000, and low Froude range ($Fr = v_r/\sqrt{gL}$, where g is gravity) of around 0.09. The high Re suggests that viscous forces in the system are vastly outweighed by inertial forces. The low Fr suggests that the robot will not generate a tall leading wave while moving. Thus, we can conclude that only form drag dominates the hull drag. Form drag depends on the pontoon geometry and grows roughly in proportion to the product of width and draft (frontal area), while yaw inertia scales approximately with the cube of pontoon length and yaw damping with its underwater lateral area. Both of these effects would slow turning and increase the thrust needed for agile maneuvers. By contrast, we expect the effective inlet width, and therefore the thruster-driven intake flow, to increase proportionally with the slenderness of the pontoon cross-section, because thinner, more streamlined bows deflect less water away from the inter-pontoon gap and create a thinner viscous boundary layer on the inner side wall. This trade-off suggests that a simple method to further increase filter intake efficiency would be to locally extend and streamline the pontoon bows into a more elliptical profile, while maintaining a shallow draft for the intended operating waters and sufficient yaw responsiveness for agile maneuvers in cluttered environments.

VIII. Summary and Future Work

In this work, we addressed the challenge of efficiently collecting microplastics, where conventional surface trawls lose efficiency to hydrodynamic resistance. We introduced a low-cost, small-scale USV for laboratory and field studies and integrated it with an undulating interfacial pump. Using a Lighthouse positioning system in a large outdoor pool, we measured the robot's speed and power consumption. Using small-scale indoor pools and a high-speed camera, we quantified the passive intake created by the robot's thrusters in a scaled towing experiment and the pump's two-dimensional flow field. We then combined these measurements in a simple numerical simulation to characterize the hydrodynamic performance of the combined pump–thruster system. These studies revealed that intermediate combinations of thruster speed and pump frequency maximize the particles captured per unit energy, and that the pontoons may yet be further optimized for improved intake flow.

Together, these findings demonstrate that active interfacial pumping can substantially improve surface microplastics collection over conventional methods. Our experimental results establish both the operating parameters and hull-design factors that can inform future design and optimization of microplastics-sampling platforms. Having demonstrated the interfacial pumping mechanism on a single robot, future work will investigate the addition of autonomous feedback control to a single robot and coordination of a team of agents to enable GPS-guided, distributed microplastics sampling and removal efforts.

References

[1] Jenna R Jambeck, Roland Geyer, Chris Wilcox, Theodore R Siegler, Miriam Perryman, Anthony Andrady, Ramani Narayan, and Kara Lavender Law. Plastic waste inputs from land into the ocean. *science*, 347(6223):768–771, 2015.

[2] Industry Agenda. The new plastics economy rethinking the future of plastics. In *World economic forum*, volume 36, 2016.

[3] Jinghan Di, Barbara K Reck, Alessio Miatto, and Thomas E Graedel. United states plastics: Large flows, short lifetimes, and negligible recycling. *Resources, Conservation and Recycling*, 167:105440, 2021.

[4] Shampa Ghosh, Jitendra Kumar Sinha, Soumya Ghosh, Kshitij Vashisth, Sungsoo Han, and Rakesh Bhaskar. Microplastics as an emerging threat to the global environment and human health. *Sustainability*, 15(14):10821, 2023.

[5] Robert C Hale, Meredith E Seeley, Mark J La Guardia, Lei Mai, and Eddy Y Zeng. A global perspective on microplastics. *Journal of Geophysical Research: Oceans*, 125(1):e2018JC014719, 2020.

[6] Qiang Zhong, Yicong Fu, Leo Liu, and Daniel B Quinn. Development of a stingray-inspired high-frequency propulsion platform with variable wavelength. In *2022 IEEE/RSJ International Conference on Intelligent Robots and Systems (IROS)*, pages 2679–2684. IEEE, 2022.

[7] Anupam Pandey, Zih-Yin Chen, Jisoo Yuk, Yuming Sun, Chris Roh, Daisuke Takagi, Sungyon Lee, and Sunghwan Jung. Optimal free-surface pumping by an undulating carpet. *Nature communications*, 14(1):7735, 2023.

[8] Soyoun Joo, Sunghwan Jung, Sungyon Lee, Robert H Cowie, and Daisuke Takagi. Freshwater snail feeding: lubrication-based particle collection on the water surface. *Journal of the Royal Society Interface*, 17(165):20200139, 2020.

[9] Gabriel Pasquier, Périne Doyen, Maria Kazour, Alexandre Dehaut, Mamadou Diop, Guillaume Duflos, and Rachid Amara. Manta net: The golden method for sampling surface water microplastics in aquatic environments. *Frontiers in Environmental Science*, 10:811112, 2022.

[10] Merel Kooi, Julia Reisser, Boyan Slat, Francesco F Ferrari, Moritz S Schmid, Serena Cunsolo, Roberto Brambini, Kimberly Noble, Lys-Anne Sirks, Theo EW Linders, et al. The effect of particle properties on the depth profile of buoyant plastics in the ocean. *Scientific reports*, 6(1):33882, 2016.

[11] Tania Montoto-Martinez, José Joaquín Hernández-Brito, and Mª Dolores Gelado-Caballero. Pump-underway ship intake: An unexploited opportunity for marine strategy framework directive (msfd) microplastic monitoring needs on coastal and oceanic waters. *PLoS One*, 15(5):e0232744, 2020.

[12] Andrea Faltynkova, Catherine E Deschênes, Artur Zolich, Martin Wagner, Tor Arne Johansen, and Geir Johnsen. Use of an uncrewed surface vehicle and near infrared hyperspectral imaging for sampling and analysis of aquatic microplastics. *Marine Pollution Bulletin*, 201:116214, 2024.

[13] Teis Schnipper, Anders Andersen, and Tomas Bohr. Vortex wakes of a flapping foil. *Journal of Fluid Mechanics*, 633:411–423, 2009.

[14] Courtney Arthur, Joel E. Baker, and Holly A. Bamford. Proceedings of the international research workshop on the occurrence, effects, and fate of microplastic marine debris, september 9-11, 2008, university of washington tacoma, tacoma, wa, usa, 2009.

[15] William Thielicke and René Sonntag. Particle image velocimetry for matlab: Accuracy and enhanced algorithms in pivlab. *Journal of Open Research Software*, 9(1), 2021.

[16] Alexander J Smits. Undulatory and oscillatory swimming. *Journal of Fluid Mechanics*, 874:P1, 2019.